Hierarchical Energy Management and Control Strategy for HydrogenElectricity Coupled DC Microgrids

Hierarchical Energy Management and Control Strategy for Hydrogen–Electricity Coupled DC Microgrids

Yang Yang, Yanjun Liu, Yuanhang Yang, Yang Li, *Senior Member*, *IEEE*, Wenchao Zhu, and Changjun Xie, *Member*, *IEEE*

***Abstract*—Hydrogen–electricity coupled DC microgrids (HE-DCMGs) represent a promising and sustainable solution for off-grid power supply. However, achieving high economic performance while ensuring DC bus voltage stability is a critically challenging task. This study proposes a hierarchical energy management and control strategy for HE-DCMGs that integrates an adaptive mutation Harris hawks optimization (AMHHO) algorithm at the system level with a fractional-order sliding mode controller (FOSMC) at the device level. A multi-objective optimization problem is formulated to minimize hydrogen consumption and reduce degradation of proton exchange membrane fuel cells and lithium-ion batteries. The AMHHO algorithm, augmented with differential evolution and Lévy flight mechanism, determines the optimal power allocation among distributed sources, while the FOSMC provides robust DC bus voltage regulation. The proposed strategy is validated on a 750 V HE-DCMG experimental platform capable of 168 hours of off-grid operation. Experimental results show that the proposed strategy reduces long-term operating costs and improves energy-utilization efficiency, achieving an overall system efficiency of 80.49%-97.37%. The DC bus voltage is maintained with a response time of 0.02 s, a low overshoot of 3.7%, and a voltage fluctuation rate of 3.08%, all of which comply with the requirements of IEEE Std 1547–2018.**

***Index Terms*—DC microgrid, hybrid energy storage system, energy management, fractional-order sliding mode controller (FOSMC), hydrogen energy storage, voltage stability.**

I. Introduction

DISTRIBUTED generation systems based on solar and wind energy have developed rapidly in recent years [1]. However, their inherent intermittency and volatility introduce significant challenges to the reliability of the power supply. Hydrogen energy storage has been recognized as a promising solution for facilitating the integration of renewable energy, owing to its high energy density, long-duration storage capability, and suitability for large-scale deployment [2]. Although hydrogen energy storage exhibits relatively low round-trip efficiency and slow dynamic response, it can be effectively complemented by electrochemical energy storage systems, which provide high energy conversion efficiency and fast transient performance. Within this context, the hydrogen–electricity coupled DC microgrid (HE-DCMG) has gained increasing attention, as it enhances the utilization of renewable energy, improves operational flexibility and stability, and supports energy transition toward low-carbon development [3].

A typical HE-DCMG consists of photovoltaic (PV) arrays, wind energy conversion systems (WECSs), proton exchange membrane fuel cells (PEMFCs), battery energy storage systems (BESSs), DC loads, and an energy management system (EMS) [4]. The EMS is essential for coordinating power flows among heterogeneous energy sources and for maintaining DC bus voltage stability under varying operating conditions [5]. A wide range of energy management and control strategies have been investigated in the literature for EMSs, including optimization-based, heuristic, and rule-based methods [6]. For instance, [7] proposed a fuzzy-logic control algorithm to retain the power balance. In [8], a hybrid scheme combining fuzzy logic and fractional-order proportional-integral-derivative (PID) control was developed to mitigate power fluctuations and improve power quality in DC microgrids. Furthermore, a barrier function-based adaptive sliding mode control algorithm was developed in [9] for AC/DC hybrid microgrids, which achieves stable operation in both grid-connected and islanded modes.

Despite significant progress, many existing EMSs do not sufficiently address multiple system-level economic objectives. Neglecting operating costs and component degradation limits their practical applicability. To overcome these shortcomings, [10] proposed a hybrid metaheuristic optimization scheme that simultaneously considers cost, environmental impact, and reliability for four standalone hybrid energy systems. In battery-integrated microgrids, [11] introduced a

Manuscript received: April 28, 2025; revised: August 25, 2025; accepted: November 25, 2025. Date of CrossCheck: November 25, 2025. Date of online publication: December 23, 2025.

This work was supported in part by the Key Supported Project of the Joint Fund for Smart Grid of the National Natural Science Foundation of China (No. U24B20103) and in part by the National Key Research and Development Project of China (No. 2020YFB1506802).

Y. Yang, Y. Liu, Y. Yang, W. Zhu, and C. Xie are with the School of Automation, Wuhan University of Technology, Wuhan 430070, China (e-mail: whutyangyang@whut.edu.cn; 348819@whut.edu.cn; yyhYYH@whut.edu.cn; zhuwenchao@whut.edu.cn; jackxie@whut.edu.cn).

Y. Li (corresponding author) is with the Department of Electrical Engineeing, Chalmers University of Technology, Gothhenburg 41296, Sweden, and he is also with the School of Electrical Engineering and Automation, Wuhan University, Wuhan 430072, China (e-mail: yangli@ieee.org).

DOI: 10.35833/MPCE.2025.000381

golden jackal optimization algorithm to minimize total operating costs. In addition, [12] developed a bi-objective optimization framework that accounts for load demand, market price variations, and renewable generation uncertainty in grid-connected microgrids. For DC hybrid microgrids incorporating PV arrays, PEMFCs, lithium-ion batteries (LIBs), and supercapacitors (SCs), [13] presented a comparative assessment of several optimization algorithms. The study reported that a Harris hawks optimization (HHO)-based external energy maximization strategy achieved superior performance in reducing hydrogen consumption and improving overall system efficiency.

However, the EMSs discussed above often overlook the critical requirement of maintaining DC bus voltage stability. In microgrid systems, stable DC bus voltage is essential [14], as voltage fluctuations degrade power quality, compromise equipment reliability, and impair overall system performance. For HE-DCMGs, this challenge is further amplified by the need for advanced control strategies that jointly consider operating costs, device aging, and physical constraints of devices [15]. Traditional single-objective algorithms, typically designed to optimize either economic performance or system stability, are limited in their ability to manage the inherent trade-offs among multiple, and sometimes conflicting, operational objectives.

To address these limitations, hierarchical energy management and control strategies, commonly referred to as hierarchical control, have been proposed and validated in various studies. For instance, [16] introduced an optimized control scheme for islanded hybrid microgrids that integrated optimization with fuzzy logic control to coordinate costs and stability objectives. In [17], a hierarchical receding horizon control framework was developed to regulate hydrogen energy storage in microgrids with wind and PV generation, effectively mitigating power fluctuations caused by renewable energy sources and improving the capability of the system to meet load demands. Reference [18] implemented a hierarchical supervisory control strategy to suppress power fluctuations in grid-connected microgrids equipped with BESSs. Furthermore, [19] presented an enhanced hierarchical model predictive control scheme for integrated microgrids involving multiple stakeholders, which achieved an effective balance between robust and economic performances.

Typically, a hierarchical energy management and control strategy comprises two distinct levels: a system level and a device level [20]. The system level operates in a centralized manner, focusing on long-term optimization to determine globally optimal power-allocation strategies. Representative approaches include economic energy management systems (EEMSs) [21], equivalent energy consumption minimization strategies [22], and frequency-decoupled or state-machine-based strategies. These approaches generate reference power commands or operating setpoints for each distributed generation unit and energy storage equipment. In contrast, the device level focuses on local, real-time control, with the primary objective of ensuring fast dynamic responses for short-term operation functions such as DC bus voltage regulation and load-following, using reference signals provided by the system level, in combination with local measurements. The coordination between the two levels is achieved through real-time reference power commands and feedback signals, enabling effective balancing of economic performance, system stability, and equipment lifespan.

Hydrogen consumption by PEMFCs represents a major contributor to operating costs, while degradation of both PEMFCs and LIBs reduces overall system efficiency and incurs higher long-term costs. Consequently, the system level must jointly optimize hydrogen usage and degradation-related costs to enhance the economic performance of HE-DCMGs. Although most existing energy management systems rely on optimization algorithms [23], they primarily emphasize minimizing hydrogen consumption costs and managing the state of charge of LIBs and SCs. Neglecting the degradation costs of PEMFCs and LIBs may lead to suboptimal energy utilization and underestimation of long-term operating costs. Incorporating degradation models can substantially improve the fidelity and accuracy of energy management optimization, but it also introduces significant computational complexity, making it challenging to obtain globally optimal solutions within practical time constraints.

The HHO algorithm employed in [13] is a bio-inspired metaheuristic technique that mimics cooperative hunting behaviors observed in nature and provides a well-balanced exploration-exploitation capability for solving complex optimization problems. However, the HHO algorithm suffers from relatively low global-exploration efficiency and limited fine-tuned exploitation accuracy [24]. To address these issues, differential evolution (DE) can be introduced, featuring mutation operations based on dynamic population differentials. This enhances population diversity and reduces the likelihood of premature convergence, though sometimes at the cost of diminished local-search precision [25]. In addition, the Lévy flight mechanism introduces random, long-distance jumps that help escape local optima and accelerate global convergence. When integrated with the DE and HHO algorithm, the Lévy flight mechanism further improves the local convergence accuracy and overall robustness of the hybrid algorithm [26].

On the other hand, the inherent volatility of renewable energy sources, dynamic load variations, uncertainties in system parameters, and stringent requirements for DC bus voltage stability demand robust and high-performance controllers at the device level. These controllers must both accurately track the optimal power references provided by the system-level energy management and ensure rapid dynamic responses. In many of the aforementioned studies, controller performance was tuned using metaheuristic algorithms to satisfy system stability and voltage regulation requirements. In contrast, the fractional-order sliding mode controller (FOSMC) offers significant advantages. It effectively suppresses overshoot and mitigates chattering, ensuring stable DC bus voltage regulation with rapid response to load variations [27]. Furthermore, FOSMC demonstrates strong robustness against disturbances and parameter uncertainties, thereby enhancing the disturbance rejection capability and dynamic reliability of the controllers.

In view of the above, this study proposes an hierarchical energy management and control strategy for an HE-DCMG that comprises PV arrays, WECS, PEMFCs, LIBs, and SCs, which integrates an adaptive mutation Harris hawks optimization (AMHHO) algorithm at the system level and an FOSMC at the device level. The proposed strategy dynamically coordinates power allocation in response to variations in load and renewable generation, aiming to simultaneously improve economic performance and ensure system stability and robustness. The main contributions of this study are summarized as follows.

1) A multi-objective optimization problem is formulated to minimize hydrogen consumption and degradation costs of PEMFC and LIB. To address this complex degradation-conscious problem, the AMHHO algorithm is developed by integrating DE and Lévy flight mechanism into the standard HHO algorithm. This enhancement can improve the balance between global exploration and local exploitation, enabling adaptive and efficient optimization of power distribution across system components throughout their lifespans.

2) An FOSMC is designed to regulate the DC bus voltage, improving dynamic response, steady-state accuracy, and disturbance rejection capability. This controller allows the system to rapidly respond to fluctuations in load demands and renewable generation while maintaining voltage stability under varying operating conditions.

The proposed strategy is implemented and validated on a 750 V HE-DCMG experimental platform. Results confirm that the integrated AMHHO algorithm and the FOSMC enhance both economic performance and DC bus voltage stability, meeting the technical requirements of IEEE Std 1547–2018 for practical deployment.

The remainder of this paper is structured as follows. Section II elaborates on the overall system architecture of the HE-DCMG and its mathematical model. Section III details the hierarchical energy management and control strategy of HE-DCMG, which encompasses system-level optimization based on the AMHHO algorithm and device-level optimization employing the FOSMC. Section IV analyzes the experimental results obtained from the HE-DCMG experimental platform and verifies the effectiveness of the proposed strategy. Finally, Section V concludes the study.

II. Overall System Configuration of HE-DCMG and Its Mathematical Model

The HE-DCMG under investigation, as illustrated in Fig. 1, comprises a renewable energy generation module and a hybrid energy storage system (HESS). The primary power supply is delivered by PV arrays and WECS within the renewable energy generation module, which are connected to the DC bus via various power converters. Due to the inherent intermittent and stochastic nature of renewable energy sources, the HE-DCMG relies on the HESS, which comprises a PEMFC, an LIB, and an SC, to mitigate supply-demand imbalances and ensure uninterrupted energy delivery [28]. In this configuration, the PEMFC converts hydrogen into electricity with water as the sole byproduct, which exhibits high efficiency and environmental sustainability [29]. The PEMFC is interfaced with the DC bus through a boost converter, while the LIB and SC are connected via respective bidirectional DC/DC converters.

To achieve optimal power allocation in the HE-DCMG under dynamic load conditions and multiple operational constraints, we propose a hierarchical energy management and control strategy that integrates the AMHHO algorithm and the FOSMC. The output power of PV arrays and WECS is controlled using respective maximum power point tracking (MPPT) algorithms to ensure efficient renewable energy harvesting and support low-carbon operation. At the system level, the AMHHO algorithm determines the power references for the PEMFC and LIB, denoted as $P_{\mathrm{FC,ref}}$ and $P_{b,\mathrm{ref}}$, respectively. The optimization objective accounts for both hydrogen consumption and degradation costs of PEMFC and LIB, which maximizes the long-term economic performance. Meanwhile, the SC operates autonomously to compensate for the short-term power mismatches and maintain load balance. At the device level, the FOSMC adjusts the duty cycle of the pulse width modulation (PWM) of power converters, which forms a closed-loop control structure that ensures DC bus voltage stability. The proposed strategy thereby ensures that the HE-DCMG operates with enhanced economic efficiency, improved transient response, and robust system operation. The rest of this section presents the optimization model used for obtaining the power references of the HESS equipment. Note that the voltage control of the PV, the current control of the WECS, and the PWM implementation of all converters shown in Fig. 1 are omitted from detailed discussion, as they are well-established techniques and are not the focus of this work.

A. PEMFC Model

1) Hydrogen Consumption Model

Based on the underlying electrochemical mechanism of PEMFCs [30], the stoichiometric ratio indicates that 1 mol of H_2 is consumed per 2 mol of electrons transferred. Thus, the molar consumption of hydrogen over a time interval Δt is calculated as:

$$n_{\mathrm{H_2}}(t)=\frac{I_{\mathrm{FC}}(t)}{2F}\Delta t=\frac{1}{2F}\frac{P_{\mathrm{FC}}(t)}{V_{\mathrm{FC}}(t)}\Delta t \tag{1}$$

where $t\in\{1,2,\ldots\}$ is the discrete time index; P_{FC}, V_{FC}, and I_{FC} are the output power, voltage, and current of the PEMFC, respectively; and $F=96485$ C/mol is the Faraday constant.

The mass of consumed hydrogen within Δt can be expressed as:

$$m_{\mathrm{H_2}}(t)=M_{\mathrm{H_2}}n_{\mathrm{H_2}}(t) \tag{2}$$

where $M_{\mathrm{H_2}}$ is the molar mass of hydrogen.

The corresponding hydrogen consumption cost of the PEMFC can be calculated as:

$$C_{\mathrm{H_2}}(t)=N_{\mathrm{cell}}m_{\mathrm{H_2}}(t)\cdot price_{\mathrm{H_2}} \tag{3}$$

where N_{cell} is the total number of cells; and $price_{\mathrm{H_2}}$ is the price of hydrogen, which is set to be 30 ¥/kg [31].

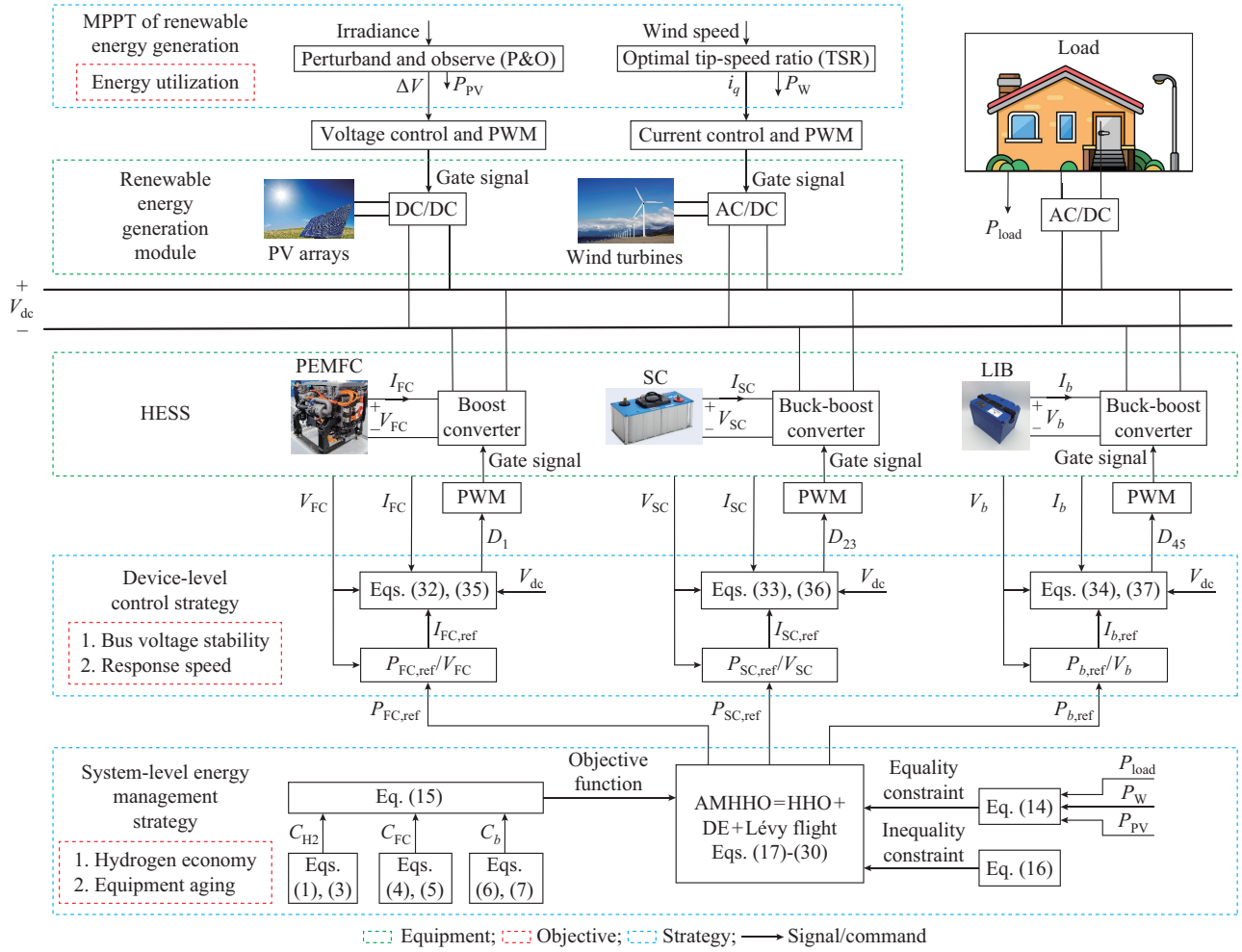

Fig. 1. Architecture of HE-DCMG under investigation.

2) Aging Model of PEMFC

During operation, variations under external environmental and operating conditions can significantly impact the service life of PEMFC [32]. According to existing studies, the degradation of PEMFC is mainly attributed to four operating conditions: load power fluctuation, high-power operation, low-power operation, and start-stop cycling [33]. To quantitatively assess the combined impact of these operating conditions on the lifespan of PEMFC, we modify a weighted empirical model proposed in [34], given as:

$$\Delta D_{\mathrm{FC}}(t)=k_p\left(d_1 T_{\mathrm{high}}(t)+d_2 T_{\mathrm{low}}(t)+d_3 N_{\mathrm{start-stop}}(t)+d_4 P_{\mathrm{change}}(t)\right) \tag{4}$$

where ΔD_{FC} is the degradation of PEMFC lifespan; T_{high} and T_{low} equal Δt when the PEMFC operates under high-power and low-power states, respectively, and zero otherwise; $N_{\mathrm{start-stop}}$ is the number of start-stop cycles, and it is set to be 1 when a start-stop cycle is identified; P_{change} is the output power fluctuation of PEMFC; d_1, d_2, d_3, and d_4 are the weighting coefficients of respective operating conditions; and k_p is a calibration coefficient.

The aging-induced cost of PEMFC can be expressed as:

$$C_{\mathrm{FC}}(t)=\frac{\Delta D_{\mathrm{FC}}(t)}{D_{\mathrm{FC,EOL}}}\cdot price_{\mathrm{FC}}\cdot P_{\mathrm{FC,max}} \tag{5}$$

where $P_{\mathrm{FC,max}}$ is the maximum rated output power of PEMFC; $price_{\mathrm{FC}}$ is the price of PEMFC, which is set to be 3000 ¥/kW [31]; and $D_{\mathrm{FC,EOL}}$ is the threshold for ΔD_{FC}, which is typically 10% [35]. The PEMFC is considered to have reached its end-of-life when cumulative degradation $D_{\mathrm{FC}}(t)=\sum_{k=1}^{t}\Delta D_{\mathrm{FC}}(k)$ increases to $D_{\mathrm{FC,EOL}}$.

By comprehensively accounting for the effects of start-stop cycles, operating conditions, and power fluctuations on PEMFC lifespan, (4) captures the long-term degradation trends of PEMFC performance with relatively low modeling complexity. This provides a foundation for subsequent multi-objective optimization at the system level.

B. Aging Model of LIB

Considering the computational burden imposed by model complexity, this study adopts a simplified empirical method, previously validated in [36], to convert the capacity loss of LIB into its expected remaining life:

$$\Delta D_b(t)=\frac{\left|P_b(t)\right|\Delta t}{2N_b Q_b} \tag{6}$$

where ΔD_b is the expected remaining life of LIB; N_b is the total number of cycles before end-of-life; Q_b is the rated capacity of LIB; and P_b is the output power of LIB. The aging-induced cost of LIB can be expressed as:

$$C_b(t)=\frac{\Delta D_b(t)}{D_{b,\mathrm{EOL}}}\cdot price_b\cdot E_b \tag{7}$$

where E_b and $price_b$ are the capacity and price (3000 ¥/kWh [31]) of LIB, respectively; and $D_{b,\mathrm{EOL}}$ is the threshold for ΔD_b, which is typically 20%. The LIB is considered to have reached its end-of-life when the cumulative capacity loss $D_b(t)=\sum_{k=1}^{t}\Delta D_b(k)$ reaches $D_{b,\mathrm{EOL}}$.

C. Renewable Energy Generation

1) PV Array

The output power of the PV array P_{PV} is closely related to the irradiance level G. The P&O method is employed for MPPT control. In the traditional P&O method, real-time monitoring of G is incorporated, and the direction and magnitude of irradiance variation are used to assist in determining the trend of power changes. The P&O method involves periodically perturbing the output voltage or current of the PV array by small amounts, observing the direction of power changes, and adjusting the operating point accordingly to progressively approach the maximum power point [37].

Based on the relationship between changes in the irradiance ΔG and changes in the output power of the PV array ΔP_{PV}, the designed power variation decision logic is as follows.

1) $\Delta G>0$ and $\Delta P_{\mathrm{PV}}>0$: this suggests that the PV array is currently operating in a region where the operating point is shifting to the right. Therefore, the output voltage of the PV array V_{PV} should be increased appropriately.

2) $\Delta G>0$ and $\Delta P_{\mathrm{PV}}<0$: this suggests that the operating point has shifted too far, and V_{PV} should be decreased.

3) $\Delta G<0$ and $\Delta P_{\mathrm{PV}}>0$: this suggests that the operating point is moving too quickly to the left, and V_{PV} should be decreased accordingly.

4) $\Delta G<0$ and $\Delta P_{\mathrm{PV}}<0$: this suggests that the operating point is likely close to the maximum power point, and a fine adjustment of V_{PV} is required.

Based on ΔG, the perturbation step size ΔV is dynamically adjusted, as defined by:

$$\Delta V=k_1\frac{|\Delta G|}{G_{\mathrm{nom}}} \tag{8}$$

where k_1 is the proportional coefficient; and G_{nom} is the nominal irradiance level, which is typically 1000 W/m^2. Through the P&O method, the system converges to a stable maximum power point, thereby achieving the optimal P_{PV} calculated by (9).

$$P_{\mathrm{PV}}=V_{\mathrm{PV}}I_{\mathrm{PV}} \tag{9}$$

where I_{PV} is the output current of the PV array.

2) WECS

For the WECS, MPPT is achieved by assuming the optimal TSR λ_{opt} is maintained, which can be expressed as:

$$\lambda_{\mathrm{opt}}=\frac{w_r R}{v_w} \tag{10}$$

where R is the rotor radius of the wind turbine; w_r is the rotational speed of the wind turbine; and v_w is the wind speed. Therefore, the electromagnetic torque of the generator T_e is adjusted to control the rotational speed of the wind turbine, aiming to reach the reference rotational speed $w_{r,\mathrm{ref}}$:

$$w_{r,\mathrm{ref}}=\frac{\lambda_{\mathrm{opt}}v_w}{R} \tag{11}$$

$$T_e=\frac{3}{2}\frac{p}{2}\psi_f i_q \tag{12}$$

where ψ_f is the rotor flux linkage; i_q is the q-axis current; and p is the number of pole pairs. The stator currents are transformed into the d-q coordinate system to calculate the d- and q-axis currents i_d and i_q. The reference d-axis current $i_{d,\mathrm{ref}}$ is set to be 0, and i_q is controlled. By adjusting i_q, the electromagnetic torque is regulated, which in turn adjusts the output power of the generator. This process allows the WECS to reach a stable maximum power point, thereby optimizing the output power of WECS P_{W} [38] as:

$$P_{\mathrm{W}}=0.5\rho A v_w^3 C_p(\lambda,\beta_1) \tag{13}$$

where ρ is the air density; A is the swept area of the wind turbine rotor; $C_p(\cdot)$ is the wind energy utilization coefficient; λ is the TSR; and β_1 is the pitch angle.

III. Hierarchical Energy Management and Control Strategy of HE-DCMG

Based on the models constructed in Section II, this section proposes a hierarchical energy management and control strategy for the HE-DCMG, aiming to achieve multiple objectives, including economy, stability, and equipment lifetime. Considering the economic and environmental sustainability of the HE-DCMG operation, the MPPT control is implemented for PV arrays and WECS to ensure their operation near the maximum power point, thereby enhancing the efficiency of renewable energy utilization while reducing reliance on conventional energy sources with carbon emissions. For the HESS, the objective function incorporates both hydrogen consumption costs and degradation costs of PEMFC and LIB. The power references of PEMFC and LIB are optimally determined via AMHHO algorithm, whereas the SC autonomously compensates for the power deficit to maintain power balance to stabilize the DC bus voltage. At the device level, FOSMC is utilized to calculate the duty cycle of DC/DC converters, allowing for closed-loop control through system feedback. The proposed strategy maximizes the operating economy while achieving the control objectives of enhancing system stability and suppressing power fluctuations.

A. System-level Energy Management Strategy

The power reference of HESS $P_{\mathrm{HESS,ref}}$ can be obtained by:

$$P_{\mathrm{HESS,ref}}(t)=P_{\mathrm{SC,ref}}(t)+P_{\mathrm{FC,ref}}(t)+P_{b,\mathrm{ref}}(t)=P_{\mathrm{load}}(t)-P_{\mathrm{PV}}(t)-P_{\mathrm{W}}(t) \tag{14}$$

where $P_{\mathrm{SC,ref}}$, $P_{\mathrm{FC,ref}}$, and $P_{b,\mathrm{ref}}$ are the reference power of SC, PEMFC, and LIB, respectively; and P_{load} is the power required by the load.

At the system level, the strategy is designed to solve (15).

$$\min_{P_{\mathrm{FC,ref}}(t),P_{b,\mathrm{ref}}(t)}\sum_{t=1}^{T}(C_{\mathrm{H_2}}(t)+C_{\mathrm{FC}}(t)+C_b(t)) \tag{15}$$

s.t.

$$\begin{cases} P_{\mathrm{FC,min}} \le P_{\mathrm{FC,ref}}(t) \le P_{\mathrm{FC,max}} \\ P_{b,\mathrm{min}} \le P_{b,\mathrm{ref}}(t) \le P_{b,\mathrm{max}} \\ SoC_{\mathrm{SC,min}} \le SoC_{\mathrm{SC}}(t) \le SoC_{\mathrm{SC,max}} \\ SoC_{b,\mathrm{min}} \le SoC_{b}(t) \le SoC_{b,\mathrm{max}} \\ 0 \le D_{\mathrm{FC}}(t) \le D_{\mathrm{FC,EOL}} \\ 0 \le D_{b}(t) \le D_{b,\mathrm{EOL}} \end{cases} \tag{16}$$

where T is the time horizon under investigation; SoC_{SC} and SoC_b are the states of charge of SC and LIB, respectively, which are obtained using the coulomb counting method; and the subscripts max and min denote the upper and lower limits of corresponding variables. This constrained optimization problem is generally nonlinear and nonconvex. The AMHHO algorithm aims to solve this optimization problem by integrating DE and Lévy flight mechanism into the standard HHO algorithm. This modification significantly improves the exploration capability of the AMHHO algorithm, mitigates premature convergence to local optima, and enhances global search efficiency. In the AMHHO algorithm, P_{FC} and P_b represent two distinct Harris hawk populations, namely the PEMFC population and the LIB population, respectively. We denote $\boldsymbol{X}_i=[P_{\mathrm{FC},i}, P_{b,i}]$ as the positions (i.e., candidate solutions) of the i^{th} hawk in its respective population, and $P_{\mathrm{FC,ref}}$ and $P_{b,\mathrm{ref}}$ as the best candidate solutions (optimal prey positions) obtained through iterative optimization within each population.

1) DE

To balance exploration and exploitation capabilities, DE is incorporated, where a nonlinear decay function is employed to adaptively control the mutation probability p_m and mutation magnitude R_m. This is achieved using an exponential adjustment mechanism, which ensures higher p_m and R_m values in the early stages to enhance global exploration, followed by a rapid decay in later stages to facilitate local exploitation. The corresponding mathematical formulation is expressed as:

$$p_m = 0.6\exp(-3n/N) + 0.1 \tag{17}$$

$$R_m = 0.4\exp(-3n/N) + 0.05 \tag{18}$$

where n denotes the current iteration index; and N is the total number of iterations. DE enhances the exploration of the search space through differential mutation operations on candidate solutions. Specifically, for each individual $\boldsymbol{X}_i$, a mutant vector can be generated according to (19).

$$\boldsymbol{X}_i(n+1) = \boldsymbol{X}_{r1}(n) + R_m(\boldsymbol{X}_{r2}(n) - \boldsymbol{X}_{r3}(n)) \tag{19}$$

where $\boldsymbol{X}_{r1}$, $\boldsymbol{X}_{r2}$, and $\boldsymbol{X}_{r3}$ are the positions of three randomly selected individuals (or hawks) from the same population.

2) Lévy Flight Mechanism

The Lévy flight mechanism is a stochastic random-walk model that enhances the ability of the AMHHO algorithm to escape local optima during global exploration [39]. This study updates the power output of individuals (candidate solutions) according to (20).

$$\boldsymbol{X}_i(n+1) = \boldsymbol{X}_i(n) + \boldsymbol{S}L_{evy} \tag{20}$$

$$L_{evy} = \frac{u}{|v|^{\frac{1}{\beta}}} \tag{21}$$

$$\sigma_u = \left(\frac{\Gamma(1+\beta)\sin\frac{\pi\beta}{2}}{\Gamma\left(\frac{1+\beta}{2}\right)\beta 2^{\frac{\beta-1}{2}}} \right)^{\frac{1}{\beta}} \tag{22}$$

where $\boldsymbol{S}$ is a random vector with elements between 0 and 1; L_{evy} denotes the step length; $u \sim \mathcal{N}(0, \sigma_u^2)$ and $v \sim \mathcal{N}(0, 1)$ are the random numbers drawn from Gaussian distributions; σ_u is the variance of the normal distribution to which u belongs; $\Gamma(\cdot)$ is the Gamma function; and β is set to be 1.5.

3) Adaptive Mutation Hybrid Strategy

The objective function (15) selects strategies between global exploration and local exploitation based on the escape uniform probability of the prey $r_0 \sim \mathcal{U}(0, 1)$ and the energy consumption E, which determines the optimal candidate solution for each iteration. The mutation operation is only performed when $r_0 \ge p_m$. The energy consumed by the prey during escape is:

$$E = 2E_0\left(1 - \frac{n}{N}\right) \tag{23}$$

where $E_0 \sim \mathcal{U}(-1, 1)$ is the initial energy. When $|E| \ge 1$, the following global exploration strategy is selected.

$$\boldsymbol{X}_i(n+1) = \begin{cases} \boldsymbol{X}_i(n) + R_m(\boldsymbol{X}_{\mathrm{ref}}(n) - \boldsymbol{X}_{r1}(n)) + R_m(\boldsymbol{X}_{r2}(n) - \boldsymbol{X}_{r3}(n)) & r_0 \ge p_m \\ \boldsymbol{X}_{\mathrm{ref}}(n) - \boldsymbol{X}_m(n) - r_4[r_5(\boldsymbol{X}_{\max} - \boldsymbol{X}_{\min}) + \boldsymbol{X}_{\min}] & r_0 < p_m \end{cases} \tag{24}$$

$$\boldsymbol{X}_m(n) = \frac{1}{M}\sum_{i=1}^{M}\boldsymbol{X}_i(n) \tag{25}$$

where $\boldsymbol{X}_{\mathrm{ref}}$ is the optimal solution in the current iteration; $\boldsymbol{X}_m$ is the average position of individuals in the current iteration; $\boldsymbol{X}_{\max}$ and $\boldsymbol{X}_{\min}$ are the upper and lower bounds of the search space, respectively; $r_i \sim \mathcal{U}(-1, 1), \forall i \in \{4, 5\}$; and M is the number of individuals in the population.

When $|E| < 1$, we adopt a local exploration strategy:

$$\boldsymbol{X}_i(n+1) = \begin{cases} \boldsymbol{Y}_i(n) & f(\boldsymbol{Y}_i(n)) \le f(\boldsymbol{X}_i(n)) \\ \boldsymbol{Z}_i(n) & f(\boldsymbol{Z}_i(n)) \le f(\boldsymbol{X}_i(n)) \end{cases} \tag{26}$$

where $f(\cdot)$ is the objective function (15); and $\boldsymbol{Y}_i$ and $\boldsymbol{Z}_i$ are the strategies selected based on r_0 and E, respectively, which determine whether to use the DE, Lévy flight mechanism, or HHO algorithm.

When $r_0 \ge p_m$, the DE is introduced:

$$\boldsymbol{Y}_i(n) = \begin{cases} \boldsymbol{X}_{\mathrm{ref}}(n) - \boldsymbol{X}_i(n) - E\left|2(1-r_6)\boldsymbol{X}_{\mathrm{ref}}(n) - \boldsymbol{X}_i(n)\right| & |E| \ge 0.5 \\ \boldsymbol{X}_{\mathrm{ref}}(n) - E\left|\boldsymbol{X}_{\mathrm{ref}}(n) - \boldsymbol{X}_i(n)\right| & |E| < 0.5 \end{cases} \tag{27}$$

$$\boldsymbol{Z}_i(n) = \boldsymbol{X}_{r1}(n) + R_m(\boldsymbol{X}_{r2}(n) - \boldsymbol{X}_{r3}(n)) \tag{28}$$

where $r_6 \sim \mathcal{U}(-1, 1)$.

When $r_0 < p_m$, the Lévy flight mechanism is introduced, and local Lévy mutation is used to replace the global Lévy flight in HHO algorithm:

$$\boldsymbol{Y}_i(n) = \begin{cases} \boldsymbol{X}_{\mathrm{ref}}(n) - E\left|2(1-r_7)\boldsymbol{X}_{\mathrm{ref}}(n) - \boldsymbol{X}_i(n)\right| & |E| \ge 0.5 \\ \boldsymbol{X}_{\mathrm{ref}}(n) - E\left|2(1-r_7)\boldsymbol{X}_{\mathrm{ref}}(n) - \boldsymbol{X}_m(n)\right| & |E| < 0.5 \end{cases} \tag{29}$$

$$\boldsymbol{Z}_i(n)=\boldsymbol{Y}_i(n)+\boldsymbol{Y}_i(n)L_{evy}(d_{im}) \tag{30}$$

where $r_7 \sim \mathcal{U}(-1, 1)$; and d_{im} is the dimension of Harris hawk population.

AMHHO algorithm adopts the adaptive mutation hybrid strategy based on the improved HHO algorithm described above to calculate the reference power $P_{\mathrm{FC,ref}}$ and $P_{b,\mathrm{ref}}$. The reference power for the SC can then be obtained based on (14).

The AMHHO algorithm is presented as Algorithm 1.

Algorithm 1: AMHHO algorithm

1. Input the HE-DCMG data and load demand
2. Determine M, N, dimension d_{im}, and search bounds in (16)
3. Initialize population matrix of size $M \times d_{im}$ by sampling uniformly within search bounds in (16)
4. **for** $n=1$ to N **do**
5. Update mutation probability p_m and mutation magnitude R_m using (17) and (18)
6. **for** each solution $\boldsymbol{X}_i$ **do**
7. Evaluate operating cost using (15)
8. Update optimal solution by comparison
9. **end for**
10. **for** each solution $\boldsymbol{X}_i$ **do**
11. Compute energy E due to the escape of prey using (23)
12. Update escape uniform probability of the prey r_0
13. **end for**
14. **if** $|E| \geq 1$ **then**
15. P_{FC} and P_b are adjusted by comparing r_0 with p_m via (24)
16. **else if** $|E| < 1$ **then**
17. **if** $r_0 \geq p_m$ **then**
18. P_{FC} and P_b are updated via (26) based on DE given by (27) and (28))
19. **else**
20. P_{FC} and P_b are updated via (26) based on Lévy flight mechanism given by (29) and (30)
21. **end if**
22. **end if**
23. **end for**
24. **Return** best variables ($P_{\mathrm{FC,ref}}$ and $P_{b,\mathrm{ref}}$) and the corresponding cost

B. Device-level Control Strategy

To mitigate the impact of the nonlinear behavior of the HE-DCMG on the bus voltage, FOSMC is employed at the device level. Meanwhile, to coordinate with the system-level energy management and to ensure that the reference power distribution determined at the system level is effectively implemented, the device level introduces current error variables for each module. A fractional-order sliding manifold is designed based on these variables, and the FOSMC-based control laws determine the duty cycles D_1-D_5 by leveraging the system state equations. D_1 is the duty cycle of the switch Q_1 in the boost converter of the PEMFC module; D_2 and D_3 are the duty cycles of the switches Q_2 and Q_3 in the buck-boost converter of the SC module, respectively; and D_4 and D_5 are the duty cycles of the switches Q_4 and Q_5 in the buck-boost converter of the LIB module. By adjusting these duty cycles, the closed-loop control enables dynamic regulation and stabilization of the bus voltage.

Here, we adopt the Caputo definition of fractional calculus. Let $y(t)$ be a function that is at least m-times differentiable. The Caputo fractional derivative is given as [40], [41]:

$${}_{t_0}^{C}D_t^{\alpha}y(t)=\frac{1}{\Gamma(m-\alpha)}\int_{\tau=t_0}^{t}\frac{y^{(m)}(\tau)}{(t-\tau)^{1+\alpha-m}}\mathrm{d}\tau \tag{31}$$

where $m=\alpha$ denotes the smallest integer that is greater than or equal to the fractional order α; and C is the plural.

To achieve the desired reference power allocation in the system-level energy management, current tracking control is implemented to ensure that the output currents (I_{FC}, I_{SC}, I_b) of the PEMFC, SC, and LIB precisely follow their respective reference currents ($I_{\mathrm{FC,ref}}=P_{\mathrm{FC,ref}}/V_{\mathrm{FC}}$, $I_{\mathrm{SC,ref}}=P_{\mathrm{SC,ref}}/V_{\mathrm{SC}}$, $I_{b,\mathrm{ref}}=P_{b,\mathrm{ref}}/V_b$, where V_{SC} and V_b are the output voltages of the SC and LIB, respectively). For the fractional-order sliding manifolds corresponding to the PEMFC, SC, and LIB, the respective fractional-order sliding surfaces are defined as:

$$s_1=\dot{e}_1+\lambda_1 e_1+\lambda_2 D^{\partial-1}e_1 \tag{32}$$

$$s_2=\dot{e}_2+\lambda_3 e_2+\lambda_4 D^{\partial-1}e_2 \tag{33}$$

$$s_3=\dot{e}_3+\lambda_5 e_3+\lambda_6 D^{\partial-1}e_3 \tag{34}$$

where $D^{\partial-1}$ denotes the Caputo fractional derivative defined in (31); λ_1-λ_6 are the constants; and $e_1=I_{\mathrm{FC}}-I_{\mathrm{FC,ref}}$, $e_2=I_{\mathrm{SC}}-I_{\mathrm{SC,ref}}$, and $e_3=I_b-I_{b,\mathrm{ref}}$ are the current tracking errors.

To control the three converters, three duty cycles D_1, D_{23}, and D_{45} are calculated based on the FOSMC [29]:

$$D_1=1+\frac{L_1}{V_{\mathrm{dc}}}\left(\dot{I}_{\mathrm{FC,ref}}+\frac{R_1}{L_1}I_{\mathrm{FC}}-\frac{V_{\mathrm{FC}}}{L_1}-\lambda_1 e_1-\lambda_2 D^{\partial-1}e_1\right)+K_1\mathrm{sgn}(s_1) \tag{35}$$

$$D_{23}=\frac{L_2}{V_{\mathrm{dc}}}\left(-\dot{I}_{\mathrm{SC,ref}}-\frac{R_2}{L_2}I_{\mathrm{SC}}+\frac{V_{\mathrm{SC}}}{L_2}+\lambda_3 e_2+\lambda_4 D^{\partial-1}e_2\right)-K_2\mathrm{sgn}(s_2) \tag{36}$$

$$D_{45}=\frac{L_3}{V_{\mathrm{dc}}}\left(-\dot{I}_{b,\mathrm{ref}}-\frac{R_3}{L_3}I_b+\frac{V_b}{L_3}+\lambda_5 e_2+\lambda_6 D^{\partial-1}e_3\right)-K_3\mathrm{sgn}(s_3) \tag{37}$$

where L_1, L_2, L_3 and R_1, R_2, R_3 correspond to the inductors and resistors in the boost converter of the PEMFC module and the buck-boost converters in the SC and LIB modules, respectively; V_{dc} is the DC bus voltage; and K_1, K_2, and K_3 are the constant control parameters. D_{23} and D_{45} are defined as:

$$D_{23}=\begin{cases}1-D_2 & \text{Boost mode}\\ D_3 & \text{Buck mode}\end{cases} \tag{38}$$

$$D_{45}=\begin{cases}1-D_4 & \text{Boost mode}\\ D_5 & \text{Buck mode}\end{cases} \tag{39}$$

IV. Experimental Validation and Result Analysis

A. Convergence Performance Comparison of AMHHO Algorithm

To systematically assess the effectiveness and robustness of the AMHHO algorithm, a representative benchmark set

was selected, including a single-peak function f_1, a multi-peak function f_{10}, and a fixed-dimension multimodal function f_{18}, as shown in Table I [24], [42], where x_i is the i^{th} input variable; and n_1 is the number of input variables. These functions are commonly used to evaluate exploration ability, exploitation capability, and performance in complex search spaces. In the table, the dimension specifies the number of variables involved in each test function, the range defines the lower and upper bounds of the decision variables, while $f_{\min}$ denotes the global minimum value of the function. The convergence behavior of AMHHO algorithm was compared with several well-established metaheuristic algorithms, namely particle swarm optimization (PSO) algorithm, whale optimization algorithm (WOA), DE algorithm, and the original HHO algorithm. The comparison was conducted in terms of the average best fitness over multiple independent runs. As illustrated in Fig. 2, the AMHHO algorithm shows faster and more stable convergence on all three benchmark functions, with 74, 74, and 10 iterations for f_1, f_{10}, and f_{18}, respectively. Furthermore, it consistently achieves the lowest final optimization error among all the algorithms. These results demonstrate that the AMHHO algorithm effectively enhances both convergence accuracy and search efficiency, supporting the use of AMHHO algorithm for solving complex energy optimization problems.

TABLE I
BENCHMARK SET

Function	Dimension	Range	$f_{\min}$
$f_1(x)=\sum_{i=1}^{n_1}x_i^2$	30	$[-100,100]$	0
$f_{10}(x)=-20\exp\left(-0.2\sqrt{\frac{1}{n_1}\sum_{i=1}^{n_1}x_i^2}\right)-\exp\left(\frac{1}{n_1}\sum_{i=1}^{n_1}\cos(2\pi x_i)\right)+20+\mathrm{e}$	30	$[-32,32]$	0
$f_{18}(x)=[1+(x_1+x_2+1)^2\cdot(19-14x_1+3x_1^2-14x_2+6x_1x_2+3x_2^2)]\cdot[30+(2x_1-3x_2)^2(18-32x_1+12x_1^2+48x_2-36x_1x_2+27x_2^2)]$	2	$[-2,2]$	3

B. Experimental Platform

An HE-DCMG experimental platform in Cixi, China is used in this study, as shown in Fig. 3. It integrates multiple energy sources, including a 100 kW WECS and a 500 kW PV array. A comprehensive EMS enables real-time monitoring and coordinated control of all subsystems. To validate the performance of the proposed strategy under islanded operation, experimental tests were conducted on this platform with a 750 V DC microgrid. In addition to the primary renewable generation capability, the platform is equipped with a 500 kW/1 MWh energy storage module and a 120 kW PEMFC module, capable of providing 168 hours ($T=168$ hours) of continuous power supply during extended power shortages.

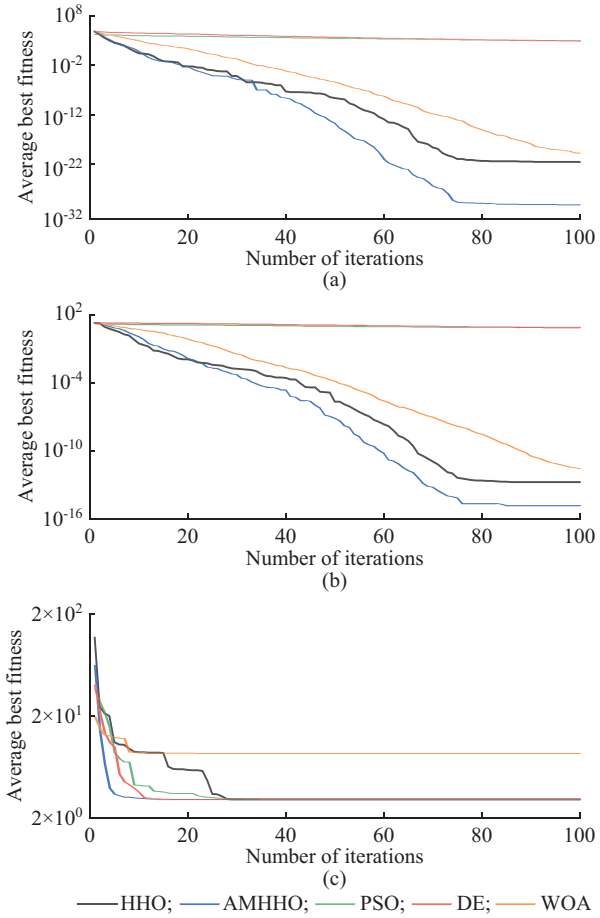

Fig. 2. Convergence performance of AMHHO algorithm compared with PSO algorithm, WOA, DE algorithm, and HHO algorithm on f_1, f_{10}, and f_{18}. (a) f_1. (b) f_{10}. (c) f_{18}.

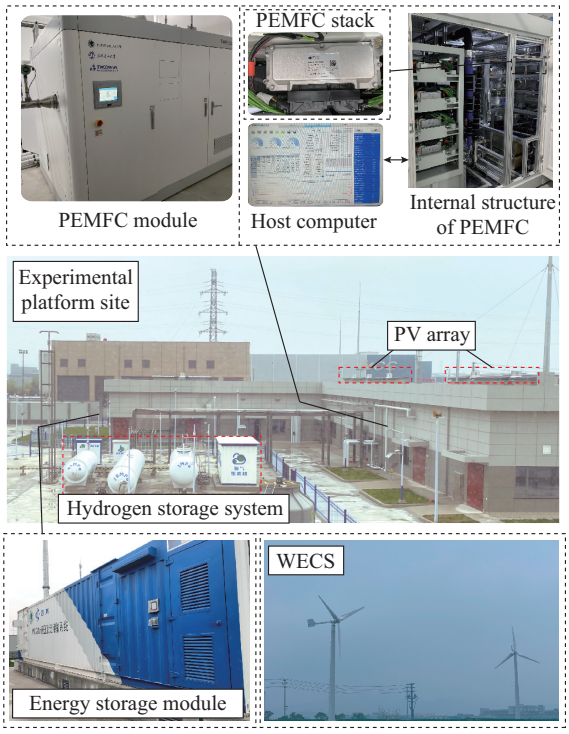

Fig. 3. HE-DCMG experimental platform in Cixi, China.

C. Performance Metrics

For practical implementation, a set of performance metrics is essential to evaluate the effectiveness of the proposed strategy. To this end, a multi-dimensional evaluation framework is established, where key economic, stability, and efficiency indicators are incorporated.

1) Economic Indicator

As indicated in (15), the total operating cost in real-time consists of three main components: the hydrogen consumption cost by the PEMFC, the aging cost of the PEMFC, and the aging cost of the LIB, expressed as:

$$C_{\text{total}}(t)=C_{\text{H}_2}(t)+C_{\text{FC}}(t)+C_b(t) \tag{40}$$

2) Stability Indicator

The dynamic response time measures how quickly the system returns to steady-state operation following load or generation fluctuations, which serves as a key indicator of dynamic stability. A shorter response time implies better system stability.

The overshoot quantifies the maximum percentage deviation by which the system output exceeds its steady-state value during the transient period. It directly reflects the degree of oscillation and system robustness.

The DC bus voltage fluctuation ratio σ is defined as the ratio between the voltage fluctuation range and the rated voltage after the system reaches a steady state:

$$\sigma=\frac{V_{\text{dc,max}}-V_{\text{dc,min}}}{V_{\text{dc,ref}}}\times 100\% \tag{41}$$

where $V_{\text{dc,max}}$ and $V_{\text{dc,min}}$ are the maximum and minimum DC bus voltages during operation, respectively; and $V_{\text{dc,ref}}=750$ V is the reference bus voltage. A smaller σ thus corresponds to better system stability.

3) Efficiency Indicator

The overall system efficiency η evaluates the energy utilization performance of the system. Higher efficiency reflects less energy waste and greater economic benefits.

$$\eta=\frac{P_{\text{load}}}{P_{\text{PV}}+P_{\text{W}}+P_{\text{FC}}+P_{\text{SC}}+P_b}\times 100\% \tag{42}$$

D. Results and Analysis

As illustrated in Fig. 4, the operational cycle is based on a representative 168-hour weekly load profile of the 750 V DC microgrid.

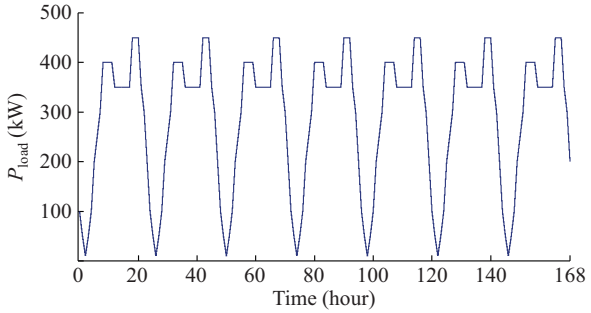

Fig. 4. Representative 168-hour weekly load profile of 750 V DC microgrid.

During the early morning (01:00-04:00), the microgrid experiences its minimum load of 10 kW. As residential demand increases, the load gradually increases, and the first daily peak of 400 kW is reached during 07:00-11:00.

A moderate reduction in load is observed during the afternoon owing to reduced residential usage during midday. The maximum daily load of 450 kW occurs during the evening peak (18:00-20:00), which coincides with increased lighting and household electricity consumption. Thereafter, the load decreases gradually as activities reduce toward nighttime.

Throughout the week, the weather conditions followed the sequence: sunny, cloudy, rainy, cloudy, cloudy, sunny, and sunny. Although solar irradiance and wind speed fluctuated over the 168-hour-long operation period, they remained relatively consistent under the same weather conditions. Figure 5 illustrates the output power of the PV array and WECS, controlled by respective MPPT algorithms, as well as the output power reference of the HESS, derived from the operating conditions given in (14) and the load profile in Fig. 4.

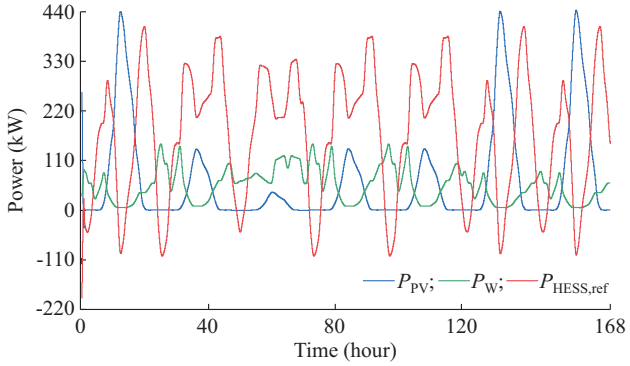

Fig. 5. Output power of PV array and WECS and output power reference of HESS.

Figure 6 illustrates the output power of different equipment in the HESS that is controlled by the proposed strategy. It can be observed that the fluctuations in P_{FC} and P_b are relatively small, consistent with the objective function that penalizes the aging effects of both the PEMFC and the LIB. The zoomed-in views for P_b and P_{FC} in Fig. 6 provide a clearer depiction of the output power variations of the LIB and the PEMFC under varying load and weather conditions.

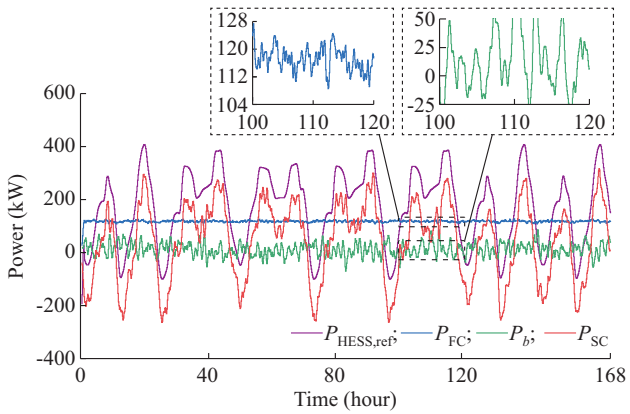

Fig. 6. Output power of different equipment in HESS.

Detailed discussions on economic, stability, and efficiency analyses are given as follows.

1) Economic Analysis

Figure 7(a) illustrates the variations in hydrogen consumption cost, the aging cost of the PEMFC, the aging cost of the LIB, and the total consumption cost over the 168-hour operation period under the proposed strategy. As shown in Figs. 6 and 7, a reduction in the output power reference of the HESS lowers the total consumption cost. Figure 7 also indicates that the aging cost of the PEMFC is the smallest among all cost components. As shown in Fig. 6, P_{FC} fluctuates within a narrow range near its rated power of 120 kW, thereby avoiding start-stop cycling or low-power operations. Therefore, the primary cause of PEMFC aging is the variation in power over time.

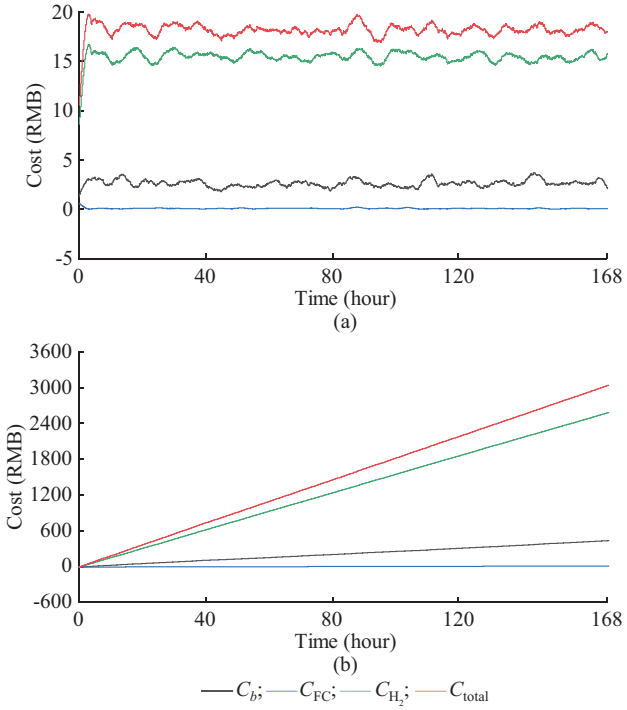

Fig. 7. Variations in hydrogen consumption cost, aging cost of PEMFC, aging cost of LIB, and total consumption cost over 168-hour operation period under proposed strategy. (a) Real-time costs. (b) Cumulative costs.

Figure 7(b) shows the cumulative costs over the 168-hour operation period. At the end of the operation period, the aging cost of the LIB is ¥441.79, the aging cost of the PEMFC is ¥15.51, the hydrogen consumption cost is ¥2581.83, and the total consumption cost is ¥3039.13. In contrast, Fig. 8(a) displays the cost variations under the EEMS. In this case, the cumulative costs increase: the aging cost of the LIB reaches ¥1337.98, the aging cost of the PEMFC reaches ¥10.14, the hydrogen consumption cost reaches ¥2649.52, and the total consumption cost reaches ¥3997.64.

Compared with EEMS, the proposed strategy reduces the total consumption cost by 23.97%. As a result, the control objective of minimizing the total consumption cost is achieved at the system level.

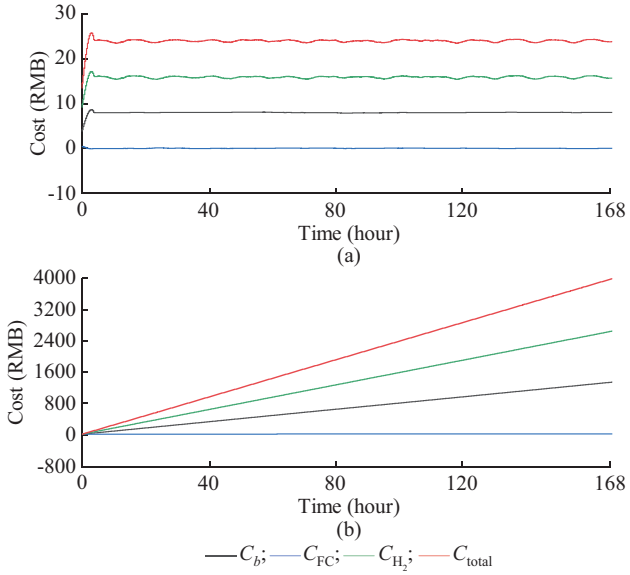

Fig. 8. Variations in hydrogen consumption cost, aging cost of PEMFC, aging cost of LIB, and total consumption cost over 168-hour operation period under EEMS. (a) Real-time costs. (b) Cumulative costs.

2) Stability Analysis

The DC bus voltage performance under the load condition in Fig. 4 is presented in Fig. 9. As shown in Fig. 9(a), the implementation of the FOSMC at the device level enables the DC bus voltage to rapidly stabilize to its reference value of 750 V. The zoomed-in view in the lower-left inset indicates a settling time of around 0.02 s with a slight overshoot of 3.7%. In Fig. 9(b), the bus voltage exhibits a maximum of 758.14 V at 70.82 hours and a minimum of 741.09 V at 146.88 hours. Based on (41), the corresponding fluctuation rate σ is calculated to be 2.27%.

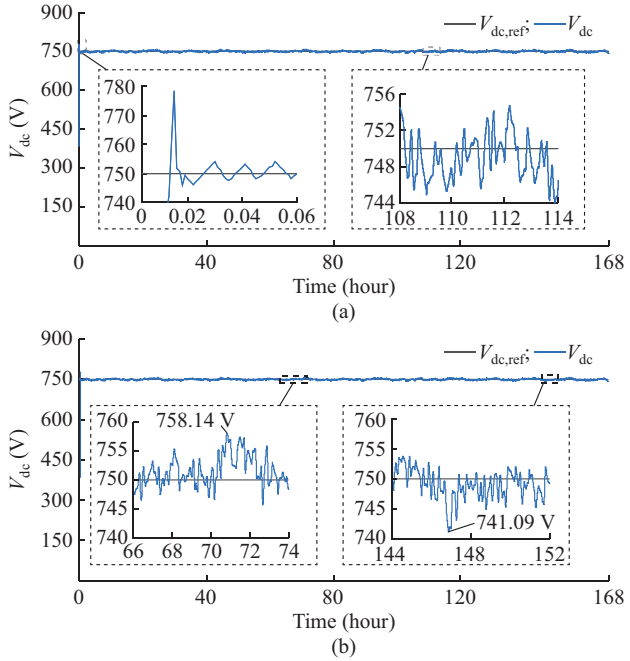

Fig. 9. DC bus voltage performance under load condition in Fig. 4. (a) Overall voltage response including start-up transient. (b) Localized waveforms around the maximum and minimum bus voltage excursions.

To further evaluate the robustness of the proposed strategy, a zero-mean, unit-variance Gaussian white noise signal, as shown in Fig. 10(a), was injected into the error signals e_1-e_3 mentioned in Section III-B. As illustrated in Fig. 10(b), the proposed strategy preserves accurate voltage tracking performance despite the introduced disturbance, with only a slight increase in the fluctuation rate of 3.08%. The settling behavior and overshoot remain essentially unaffected, indicating the strong disturbance-rejection capability of the proposed strategy.

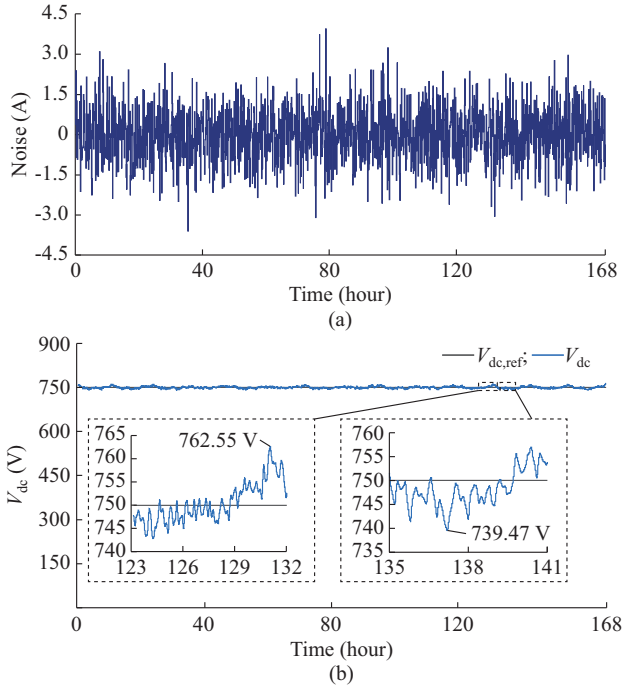

Fig. 10. DC bus voltage performance with a white noise disturbance under load condition in Fig. 4. (a) Injected zero-mean, unit-variance Gaussian white noise signal. (b) Resulting bus voltage waveform.

The above results confirm that the FOSMC has fast dynamic response while effectively suppressing voltage overshoot. Even in the presence of disturbances, the controller maintains the bus voltage fluctuation rate within 3.08%, which demonstrates its control capability of robust voltage stability under complex operating conditions and strong disturbance rejection capability against random perturbations. Moreover, the achieved voltage fluctuation rate meets the IEEE Std 1547−2018 [43] that requires a voltage deviation of no more than 5%, further validating the practical applicability of the proposed strategy.

3) Efficiency Analysis

Under the operating conditions in Fig. 4, the system efficiency obtained using the proposed strategy is depicted in Fig. 11. After reaching steady-state conditions, the efficiency ranges from 80.49% to 97.37%. In particular, the highest efficiency is achieved when the load falls within the range of 50%-70%. In contrast, when the load drops below 30%, the system efficiency decreases accordingly. Furthermore, Fig. 12 illustrates the percentage contributions of different power sources to the total absorbed and emitted power. The value larger than 0 represents the contribution to the emitted power, while the value smaller than 0 represents the contribution to the absorbed power. It can be observed that when the load reaches its peak, all power sources supply power to the load. Conversely, during load valleys, the energy storage equipment (LIB and SC) is charged by the remaining power sources, coinciding with a decline in system efficiency.

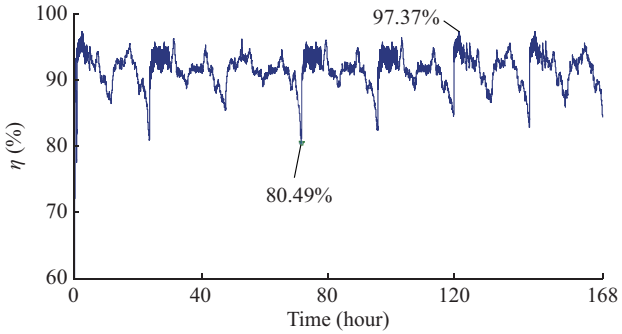

Fig. 11. System efficiency obtained using the proposed strategy under operating conditions in Fig. 4.

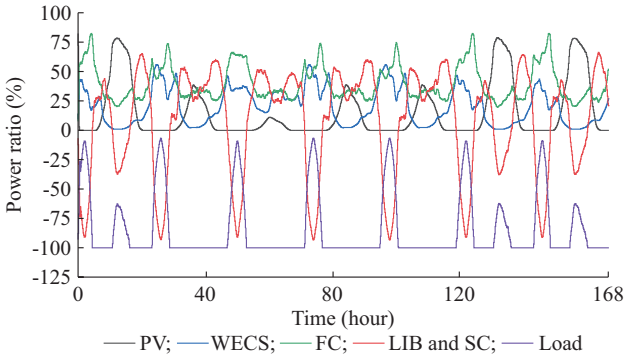

Fig. 12. Percentage contributions of different power sources to total absorbed and emitted power.

In summary, the experimental results are found to be well-aligned with the theoretical expectations. Under the selected benchmark test functions, the AMHHO algorithm exhibits the fastest convergence speed with the smallest convergence error among other optimization algorithms such as HHO, PSO, DE, and WOA, making it an effective and applicable solution.

The proposed strategy, which combines the aging- and cost-aware power allocation strategy via the AMHHO algorithm with the robust control capability of FOSMC, effectively balances economic performance with system efficiency. The AMHHO algorithm ensures economic power dispatch at the system level, while the FOSMC expands the control scope to accommodate highly nonlinear dynamics, thereby maintaining high voltage stability and ensuring control adaptability under varying load and power source conditions.

V. Conclusion

This paper proposes a hierarchical energy management and control strategy for HE-DCMGs, which is validated on an experimental platform of a 750 V DC microgrid. The proposed strategy integrates an AMHHO algorithm for system-level economic optimization and an FOSMC for device-level voltage regulation. The AMHHO algorithm effectively ad-

dresses a multi-objective nonlinear optimization problem that considers the aging costs of fuel cells and LIBs at the system level. By combining DE and Lévy flight mechanism, the proposed strategy dynamically adapts to varying conditions such as solar irradiance, wind speed, and load demand, which enables economically efficient power dispatch. At the device level, the FOSMC ensures voltage stability with a fast dynamic response, achieving a settling time of 0.02 s, an overshoot of less than 3.7%, and a voltage fluctuation of within 3.08%, in compliance with IEEE Std 1547–2018. The proposed strategy enhances both economic performance and system stability, with steady-state energy efficiency ranging from 80.49% to 97.37%. Future work will focus on the real-time implementation and scalability of larger, interconnected microgrids.

In practical deployments, the pressure threshold of the hydrogen energy storage tank has a significant impact on the economic analysis of the system. The research covered in this paper relies on real-time feedback from the system, which places high demands on the system communication equipment and increases infrastructure costs. In the future, we will use advanced deep reinforcement learning to dynamically optimize hydrogen energy storage and combine it with machine learning-based predictive control to over-predict load, PV, and wind power to generate optimization commands in advance, which will further improve the system economics, response speed, and robustness to sudden changes under operating conditions.

REFERENCES

[1] M. Thulasingam and A. D. V. R. Periyanayagam, "Radial distribution systems performance enhancement through RE (renewable energy) integration and comprehensive contingency ranking analysis," *Green Energy and Intelligent Transportation*, vol. 4, no. 1, p. 100245, Feb. 2025.

[2] T. Khan, M. Yu, and M. Waseem, "Review on recent optimization strategies for hybrid renewable energy system with hydrogen technologies: state of the art, trends and future directions," *International Journal of Hydrogen Energy*, vol. 47, no. 60, pp. 25155-25201, Jul. 2022.

[3] B. Du, Y. Peng, Y. Li *et al*., "Compatible matching and synergy operation optimization of hydrogen-electric hybrid energy storage system in DC microgrid," *Energy Conversion and Management*: *X*, vol. 26, p. 101014, Apr. 2025.

[4] S. Ishaq, I. Khan, S. Rahman *et al*., "A review on recent developments in control and optimization of micro grids," *Energy Reports*, vol. 8, pp. 4085-4103, Nov. 2022.

[5] M. Mishra, B. Patnaik, M. Biswal *et al*., "A systematic review on DC-microgrid protection and grounding techniques: issues, challenges and future perspective," *Applied Energy*, vol. 313, p. 118810, May 2022.

[6] L. Ahmethodžić, M. Musić, and S. Huseinbegović, "Microgrid energy management: classification, review and challenges," *CSEE Journal of Power and Energy Systems*, vol. 9, no. 4, pp. 1425-1438, Jul. 2023.

[7] G. Bharathi, P. Kantharao, and R. Srinivasarao, "Fuzzy logic control (FLC)-based coordination control of DC microgrid with energy storage system and hybrid distributed generation," *International Journal of Ambient Energy*, vol. 43, no. 1, pp. 4255-4271, Jan. 2022.

[8] A. A. A. Alahmadi, Y. Belkhier, N. Ullah *et al*., "Hybrid wind/PV/battery energy management-based intelligent non-integer control for smart DC-microgrid of smart university," *IEEE Access*, vol. 9, pp. 98948-98961, Jul. 2021.

[9] A. Armghan, M. Hassan, H. Armghan *et al*., "Barrier function based adaptive sliding mode controller for a hybrid AC/DC microgrid involving multiple renewables," *Applied Sciences*, vol. 11, no. 18, p. 8672, Jan. 2021.

[10] W. Zhang and A. Maleki, "Modeling and optimization of a stand-alone desalination plant powered by solar/wind energies based on back-up systems using a hybrid algorithm," *Energy*, vol. 254, p. 124341, Sept. 2022.

[11] R. P. Kumar and G. Karthikeyan, "A multi-objective optimization solution for distributed generation energy management in microgrids with hybrid energy sources and battery storage system," *Journal of Energy Storage*, vol. 75, p. 109702, Jan. 2024.

[12] M. Rawa, A. Abusorrah, Y. Al-Turki *et al*., "Efficient energy management framework for enhancing the techno-economic-environmental performance of grid-connected microgrids under uncertain conditions," *Ain Shams Engineering Journal*, vol. 15, no. 1, p. 102336, Jan. 2024.

[13] H. Rezk and A. Fathy, "Hydrogen reduction-based energy management strategy of hybrid fuel cell/PV/battery/supercapacitor renewable energy system," *Journal of Energy Storage*, vol. 86, p. 111316, May 2024.

[14] A. Shafiqurrahman, V. Khadkikar, and A. K. Rathore, "Electric vehicle-to-vehicle (V_2V) power transfer: electrical and communication developments," *IEEE Transactions on Transportation Electrification*, vol. 10, no. 3, pp. 6258-6284, Sept. 2024.

[15] A. Pepiciello, C. Bernardo, and J. L. Domínguez-García, "Modeling of multi-energy systems as multilayer networks," in *Proceedings of 2023 IEEE Belgrade PowerTech*, Belgrade, Serbia, Jun. 2023, pp. 1-6.

[16] S. A. Shezan, M. F. Ishraque, G. Shafiullah *et al*., "Optimization and control of solar-wind islanded hybrid microgrid by using heuristic and deterministic optimization algorithms and fuzzy logic controller," *Energy Reports*, vol. 10, pp. 3272-3288, Nov. 2023.

[17] M. B. Abdelghany, A. Al-Durra, H. Zeineldin *et al*., "Integration of cascaded coordinated rolling horizon control for output power smoothing in islanded wind-solar microgrid with multiple hydrogen storage tanks," *Energy*, vol. 291, p. 130442, Mar. 2024.

[18] G. Wen, J. Xu, and Z. Liu, "Hierarchical regulation strategy for smoothing tie-line power fluctuations in grid-connected microgrids with battery storage aggregators," *IEEE Transactions on Industrial Informatics*, vol. 20, no. 10, pp. 12210-12219, Oct. 2024.

[19] Z. Zhao, J. Xu, Y. Lei *et al*., "Robust dynamic dispatch strategy for multi-uncertainties integrated energy microgrids based on enhanced hierarchical model predictive control," *Applied Energy*, vol. 381, p. 125141, Mar. 2025.

[20] D. Y. Yamashita, I. Vechiu, and J. P. Gaubert, "A review of hierarchical control for building microgrids," *Renewable and Sustainable Energy Reviews*, vol. 118, p. 109523, Feb. 2020.

[21] H. Rezk, A. M. Nassef, M. A. Abdelkareem *et al*., "Comparison among various energy management strategies for reducing hydrogen consumption in a hybrid fuel cell/supercapacitor/battery system," *International Journal of Hydrogen Energy*, vol. 46, no. 8, pp. 6110-6126, Jan. 2021.

[22] H. Rezk and A. M. Eltamaly, "A comprehensive comparison of different MPPT techniques for photovoltaic systems," *Solar Energy*, vol. 112, pp. 1-11, Feb. 2015.

[23] Z. Chen, Z. Li, D. Lin *et al*., "Multi-time-scale optimal scheduling of integrated energy system with electric-thermal-hydrogen hybrid energy storage under wind and solar uncertainties," *Journal of Modern Power Systems and Clean Energy*, vol. 13, no. 3, pp. 904-914, May 2025.

[24] A. A. Heidari, S. Mirjalili, H. Faris *et al*., "Harris Hawks optimization: algorithm and applications," *Future Generation Computer Systems*, vol. 97, pp. 849-872, Aug. 2019.

[25] X. Wang and X. Yu, "Differential evolution algorithm with three mutation operators for global optimization," *Mathematics*, vol. 12, no. 15, p. 2311, Jan. 2024.

[26] X. Liu, Q. Zhang, H. Xi *et al*., "Reinforcement learning-based differential evolution algorithm with Lévy flight," in *Bio-Inspired Computing: Theories and Applications*, Singapore: Springer Nature, 2024, pp. 142-156.

[27] Y. Yang, Y. Yang, C. Xie *et al*., "A hierarchical energy management strategy for DC microgrid hybrid energy storage systems based on fractional-order sliding mode controller," *Journal of Energy Storage*, vol. 99, p. 113307, Oct. 2024.

[28] K. B. Samal, S. Pati, and R. Sharma, "Power management using an improved EMS algorithm in a stand-alone hybrid PV-PEMFC microgrid with reduced converter count," *Green Energy and Intelligent Transportation*, doi: 10.1016/j.geits.2025.100302

[29] B. Chen, R. Ma, Y. Zhou *et al*., "Co-optimization of speed planning and cost-optimal energy management for fuel cell trucks under vehicle-following scenarios," *Energy Conversion and Management*, vol. 300, p. 117914, Jan. 2024.

[30] Z. Zhou, Z. Fu, L. Zhang *et al*., "Multi-objective optimization for low hydrogen consumption and long useful life in fuel cell emergency power supply systems," *International Journal of Hydrogen Energy*, vol. 68, pp. 297-310, May 2024.

[31] W. Zou, J. Li, Q. Yang *et al.*, "A real-time energy management approach with fuel cell and battery competition-synergy control for the fuel cell vehicle," *Applied Energy*, vol. 334, p. 120667, Mar. 2023.
[32] Y. Liu, H. Li, Y. Yang *et al.*, "Reliability assessment of PEMFC aging prediction based on probabilistic Bayesian mixed recurrent neural networks," *Renewable Energy*, vol. 246, p. 122892, Jun. 2025.
[33] Z. Sun, Y. Wang, Z. Chen *et al.*, "Min-max game based energy management strategy for fuel cell/supercapacitor hybrid electric vehicles," *Applied Energy*, vol. 267, p. 115086, Jun. 2020.
[34] X. Huang, J. Zhang, K. Ou *et al.*, "Deep reinforcement learning-based health-conscious energy management for fuel cell hybrid electric vehicles in model predictive control framework," *Energy*, vol. 304, p. 131769, Sept. 2024.
[35] H. Chen, P. Pei, and M. Song, "Lifetime prediction and the economic lifetime of proton exchange membrane fuel cells," *Applied Energy*, vol. 142, pp. 154-163, Mar. 2015.
[36] S. Ebbesen, P. Elbert, and L. Guzzella, "Battery state-of-health perceptive energy management for hybrid electric vehicles," *IEEE Transactions on Vehicular Technology*, vol. 61, no. 7, pp. 2893-2900, Sept. 2012.
[37] N. Femia, G. Petrone, G. Spagnuolo *et al.*, "Optimization of perturb and observe maximum power point tracking method," *IEEE Transactions on Power Electronics*, vol. 20, no. 4, pp. 963-973, Jul. 2005.
[38] A. Fathy, "Bald eagle search optimizer-based energy management strategy for microgrid with renewable sources and electric vehicles," *Applied Energy*, vol. 334, p. 120688, Mar. 2023.
[39] Y. Liu and B. Cao, "A novel ant colony optimization algorithm with Lévy flight," *IEEE Access*, vol. 8, pp. 67205-67213, Apr. 2020.
[40] F. Lin, M. Huang, S. Chen *et al.*, "Adaptive backstepping control for synchronous reluctance motor based on intelligent current angle control," *IEEE Transactions on Power Electronics*, vol. 35, no. 7, pp. 7465-7479, Jul. 2020.
[41] N. Sun, D. Liang, Y. Wu *et al.*, "Adaptive control for pneumatic artificial muscle systems with parametric uncertainties and unidirectional input constraints," *IEEE Transactions on Industrial Informatics*, vol. 16, no. 2, pp. 969-979, Feb. 2020.
[42] N. Zeng, Z. Wang, W. Liu *et al.*, "A dynamic neighborhood-based switching particle swarm optimization algorithm," *IEEE Transactions on Cybernetics*, vol. 52, no. 9, pp. 9290-9301, Sept. 2022.
[43] *IEEE Standard for Interconnection and Interoperability of Distributed Energy Resources with Associated Electric Power Systems Interfaces*, Revision of IEEE Std 1547–2018, 2018.

Yang Yang received the Ph.D. degree in power engineering and engineering thermophysics from Wuhan University of Technology, Wuhan, China, in 2024. Since 2022, she has been an Associate Professor with the School of Automation, Wuhan University of Technology. Her research interests include state estimation, aging prediction of fuel cells and lithium batteries, energy management of hybrid energy storage system, and new-type power system energy storage.

Yanjun Liu is currently pursuing the M.S. degree in electrical engineering at the School of Automation, Wuhan University of Technology, Wuhan, China. His current research interests include prognostics health management of fuel cells, state estimation, and neural network.

Yuanhang Yang is currently pursuing the M.S. degree in electrical engineering at the School of Automation, Wuhan University of Technology, Wuhan, China. Her current research interests include direct current microgrid, hierarchical energy management strategy, and hybrid energy storage system.

Yang Li received the B.E. degree in electrical engineering from Wuhan University, Wuhan, China, in 2007, and the M.Sc. and Ph.D. degrees in power engineering from Nanyang Technological University (NTU), Singapore, in 2008 and 2015, respectively. He was with the Energy Research Institute, NTU, the School of Electrical Engineering and Computer Science, Queensland University of Technology, Brisbane, Australia, the School of Automation, Wuhan University of Technology, Wuhan, China, the Department of Electrical Engineering, Chalmers University of Technology, Gothenburg, Sweden. He is currently a Professor with the School of Electrical Engineering and Automation, Wuhan University, Wuhan, China. His research interests include modeling, control, and application of renewable and energy storage systems in power systems and transport sectors.

Wenchao Zhu received the Ph. D. degree in power engineering and engineering thermophysics from the Wuhan University of Technology, Wuhan, China, in 2023. He is currently an Assistant Researcher with the Automotive Engineering College of Wuhan University of Technology, Wuhan, China. From 2022 to 2023, he received funding from the China Scholarship Council and became a joint Ph.D. student with Nanyang Technological University, Singapore. His research interests include new energy management technology and thermoelectric power generation technology.

Changjun Xie received the Ph. D. degree in vehicle engineering from the Wuhan University of Technology (WHUT), Wuhan, China, in 2009. He is currently a Professor with the School of Automation, WHUT. He is the Dean of the Outstanding Engineers College, WHUT. From 2012 to 2013, he was a Visiting Scholar with the University of California Davis, Davis, USA. His research interests include fuel cell system, control strategy of new vehicles, and new-type power system energy storage.